COMMUNICATIONS IN NUMERICAL METHODS IN ENGINEERING
Commun. Numer. Meth. Engng (2009)
Published online in Wiley InterScience (www.interscience.wiley.com). DOI: 10.1002/cnm.1298

Effects of flow vortex on a chorded mitral valve in the left ventricle

M. Yin[1], X. Y. Luo[2,*,†], T. J. Wang[1] and P. N. Watton[3]

[1]*MOE Key Laboratory for Strength and Vibration, Xi'an Jiaotong University, People's Republic of China*
[2]*Department of Mathematics, University of Glasgow, U.K.*
[3]*Institute of Biomedical Engineering, Department of Engineering Science, University of Oxford, U.K.*

SUMMARY

An Immersed Boundary fluid–structure interaction model is developed to investigate the dynamic behaviour of a prosthetic chorded mitral valve (MV) inside the left ventricle (LV). In order to simulate more realistic physiological flow conditions, *in vivo* magnetic resonance images of the LV are used to determine the anatomical structure and the motion of the LV. The LV geometry and its motion are incorporated into the dynamic MV model. This model allows us to investigate the influences of the flow vortex generated by the LV motion on the MV dynamics, as well as the impact of the motion of the chordae attachment points (CAPs). Results are compared with two other cases: (i) an LV model with no prescribed motion of the CAPs, (ii) a Tube model in which the LV is replaced by a tube, although the motion of the chordae is incorporated. These special cases enable the influence of the chordae motion and the vortex on the behaviour of the MV to be analysed independently. It is found that when the MV is placed inside a dynamic LV, the chordae and the valve stretch are significantly increased in the commissural region, and the flow field is strongly asymmetric, with a clockwise single vortex appearing after the early rapid filling phase of the diastole. Given that we impose a flow rate boundary condition, the reverse pressure gradient cannot be established and, hence, the valve does not close properly. Clearly, the presence of the flow vortex alone is not strong enough to aid the valve closure.

Received 12 February 2009; Revised 15 May 2009; Accepted 29 May 2009

KEY WORDS: immersed boundary; fluid–structure interactions; mitral valve; prosthetic heart valve; vortex; left ventricle; chordae

1. INTRODUCTION

The heart consists of four chambers, two atria (upper chambers) and two ventricles (lower chambers). Blood must pass through a valve to exit each of the chambers. The exit of each chamber

*Correspondence to: X. Y. Luo, Department of Mathematics, University of Glasgow, U.K.
†E-mail: x.y.luo@maths.gla.ac.uk

Contract/grant sponsor: British Heart Foundation
Contract/grant sponsor: Royal Society
Contract/grant sponsor: Royal Academy of Engineering

has a valve that functions to prevent the backward flow of blood. The tricuspid and pulmonary valves control the exit of blood from the right atria and ventricle, respectively. The mitral valve (MV) is located between the left atrium and the left ventricle (LV), and the aortic valve is located between the LV and the aorta. Each year there are 225 000 valve replacements performed world wide. Among the four valves, the MV and aortic valve are usually more affected by diseases due to the higher pressure that they are subjected to.

Compared with the aortic valves, the MV has been understudied due to its complex anatomical structure. It consists of two geometrically distinct flexible leaflets, a mitral annulus and chordae tendinae that connect the valve leaflets to the papillary muscles [1], which are located in the walls of the ventricle. The chordae act to reinforce the leaflet structure and prevent prolapse of the leaflets when the valve closes. In addition, they also assist in maintaining the geometry and functionality of the ventricle.

There are two typical diseases of the MV, i.e. mitral stenosis and mitral regurgitation. Mitral stenosis, which is generally the result of rheumatic heart disease [2, 3], is characterized by a thickening of valve; this results in the valve not opening fully during diastole. Mitral regurgitation is caused by MV prolapse, floppy MV, and other heart diseases resulting un-coordination of the valve leaflets [4, 5]. In this disease, the valve cannot close properly and blood leaks into the left atria during systole. When either of these diseases become severe, mitral replacements with either mechanical or prosthetic valves are often necessary.

The most ideal replacement should simulate the natural mitral complex (mitral annulus, leaflets, chordae, papillary muscles) as closely as possible. However, to date, all replacement valves in clinical use, mechanical or bioprosthetic, have been designed for the aortic valve position. These valves are simply put in the reversed position for the MV replacement. Potentially, this has significant long-term effects on ventricle pathology due to the loss of functional chordae. Furthermore, the replacement of the asymmetric geometry of the MV by the symmetric aortic valve configuration will also alter the vortex structures that develop as the blood flows through the valve and fills the ventricle. This may have deleterious hemodynamic consequences. In fact, it has been shown clinically that the durability of porcine valves is less with mitral bioprostheses than with aortic bioprostheses [6, 7]. The more rapid deterioration of mitral bioprostheses may be due to higher ventricular systolic pressures against the mitral cusps as compared with the diastolic pressures resisted by aortic bioprosthetic leaflets.

Both experimental and computational analysis can guide prosthesis design; however, the advantage of computational analysis is that material and geometric parameters can be easily changed to determine an optimum design. The focus of our research is to evaluate the optimal design of prosthetic MVs and guide experimental analysis and design. Computational modelling of the MV is highly challenging: the geometry of the chordae and leaflets is complex; the dynamic motion of the LV causes a displacement of the papillary muscle base relative to the mitral annulus; the papillary muscles contract and relax during the cardiac cycle; the geometry of the mitral annulus is dynamic and so on. Furthermore, large deformation fluid–structure interactions are present during opening and closing phases.

Several groups have developed effective three-dimensional structural finite element models of the human MV. Kunzelman and co-workers were the first to use this approach and have adopted it to the widest extent, either to mimic normal mitral function [8, 9] or to understand the biomechanics underlying valvular diseases [10–12] and surgical corrections [13–15]. Lim *et al.* [16] and Prot *et al.* [17] studied normal mitral function. Maisano *et al.* [18] and Votta *et al.* [19, 20] used FE models to analyse the effects of annuloplasty procedures. The biomechanical

DOI: 10.1002/cnm

response of the valve to the Alfieri stitch technique was reported by Votta *et al.* [20] and Dal Pan *et al.* [21].

Recently, the dynamic performance of a bioprosthetic MV has been studied by the present authors [22, 23]. In these studies, the dynamic behaviour of a chorded mitral prosthesis was modelled using the immersed boundary (IB) method, which accounts for the coupled fluid–structure interactions of the blood flow and the MV leaflets. The IB model was developed to analyse the performance of the valve within an experimental rig. The valve was housed in a rigid cylindrical tube and a periodic flow profile was prescribed consistent with experimental measurements. Although the geometry of the ventricle was not considered, the relative motions of the mitral annulus and the chordal attachment points (CAPs) with respect of the annulus were incorporated into the computational simulation. This motion was determined by analysing high resolution MRI data from a normal human ventricle, and used as the specified boundary condition. While the simulations successfully predicted the dynamic performance of the mitral design and suggested potential improvements in future designs, they could not analyse the influence of the vortex generated by the LV on the behaviour of the valve.

MV fluid dynamics studies using magnetic resonance imaging have shown that a large anterior vortex is normally present at the onset of partial valve closure, as well as following the atrial contraction [24]. Bellhouse [25] first suggested that vortices generated by the ventricular filling aid the partial closure of the MV following early diastole, and that without the strong outflow tract vortices, the valve would remain open at the onset of ventricular contraction. However, later *in vitro* experiments suggested that both flow deceleration and partial valve closure were due to an adverse pressure differential in mid-diastole, even in the absence of a ventricular vortex [26, 27]. Thus, although the vortices may provide additional closing effects in the initial stage, the adverse pressure gradient appears to be dominant in the MV closure. A more unified theory of valve closure includes the importance of chordal tension, flow deceleration, and ventricular vortices, with chordal tension being a necessary condition for the other two [28]. Baccani *et al.* [29] studied the left LV filling phase using an axis-symmetric numerical model, though their LV is assumed to be a prolate spheroid, and the MV is replaced by a thin circular orifice. Long *et al.* [30] investigated subject-specific left LV flow based on MRI, and revealed some interesting flow features. They found that a swirling flow pattern was generated at the beginning of systole, and in the slow filling phase of the diastole, a main vertex was established. Clearly, the whole flow field was strongly asymmetric throughout the cycle; though as in Baccani *et al.* [29], they used adjusting orifice areas to mimic the effects of the aortic valve and MV during the dynamic cycle.

In this paper, the MV model is extended to include the effect of the dynamic motion of the whole LV. Thus the difference between this study and their earlier ones is that a realistic-designed MV is present, which enables us to see the interaction between the valve and the moving LV. The IB method is used to describe the fluid–structure interactions between the blood flow and the MV leaflets. The motion of LV is extracted from the *in vivo* MRI data of a healthy subject. The simulation shows that the vortex has a strong influence on the mechanical behaviour of the valve. The results are compared with the two other cases: the Tube model, in which the LV is replaced by a tube, and the LV Fixed-CAP model, in which the chordae positions are fixed in space relative to the mitral annulus, although the MV is still placed in a moving ventricle. The main observation is that the presence of the ventricle model changes the flow significantly; it introduces a strong vortex and makes the valve deformation greater and highly asymmetric. However, the simulation suggests that the vortex flow induced by the LV does not necessarily assist valve closure.

DOI: 10.1002/cnm

2. METHODS

2.1. The IB method [*31–34*]

The IB method considers the interaction of a viscous incompressible fluid with an immersed system of elastic fibers. The geometry and stiffness of the fibres are constructed to represent the elastic body to be modelled. A fixed Eulerian lattice, $\mathbf{x}=(x_1, x_2, x_3)$, describes the fluid, and a freely moving Lagrangian lattice, $\mathbf{r}=(r_1, r_2, r_3)$, describes the elastic material. Elastic fibres move at the local fluid velocity and apply force locally to the fluid in which they immersed. The interaction between the fluid and structure is achieved by distributing an inhomogeneous forcing term onto the fluid domains, and interpolating the velocity of the elastic body from neighbouring fluid nodes near the fluid–structure interface.

The Lagrangian form of the elastic fibre point force density applied by the fibres to the fluid is

$$F(\mathbf{r}, t)=\frac{\partial}{\partial s}(T\tau) \tag{1}$$

where T represents the tension within the fibre (which may be a nonlinear function of the fibre strain), τ is the unit tangent vector to the fibres, s is the arc length, and t denotes time.

The nodal force density needs to be distributed to the fluid and is expressed in terms of the Eulerian variables. This is achieved by expressing it as the convolution of the fibre force density with a delta function

$$f(\mathbf{x}, t)=\int_{\Gamma_s} F(\mathbf{r}, t)\delta(\mathbf{x}-X(\mathbf{r}, t))\,\mathrm{d}s \tag{2}$$

where $f(\mathbf{x}, t)$ is the force density applied by the fibre to the fluid at time t and δ is the three-dimensional Dirac delta function $\delta(\mathbf{x})=\delta(x_1)\delta(x_2)\delta(x_3)$. The integral is performed over the entire system of fibres.

The Navier–Stokes equations govern the motion of the fibre-reinforced viscous incompressible fluid, i.e.

$$\rho\left(\frac{\partial \mathbf{u}}{\partial t}+\mathbf{u}\times\nabla\mathbf{u}\right)+\nabla p=\mu\nabla^2\mathbf{u}+f, \quad \nabla\times\mathbf{u}=0 \tag{3}$$

where $\mathbf{u}(\mathbf{x}, t)$ is the fluid velocity, $p(\mathbf{x}, t)$ is the fluid pressure, and ρ and μ represent the fluid density and viscosity, respectively.

The no-slip condition of a viscous fluid implies that the fibres move at the same velocity as neighbouring fluid particles along the fluid–structure interface and thus

$$u(\mathbf{X}(\mathbf{r}, t))=\frac{\partial \mathbf{X}(\mathbf{r}, t)}{\partial t}=\int \mathbf{u}(\mathbf{x}, t)\delta(x-\mathbf{X}(\mathbf{r}, t))\,\mathrm{d}\mathbf{x} \tag{4}$$

where $\mathbf{u}(\mathbf{X}(\mathbf{r}, t))$ is the velocity of the fibres.

Equations (1)–(4) completely specify the system. The incompressible viscous Navier–Stokes equations are discretized on a fixed Eulerian lattice, while the elastic fibre equations are discretized on a moving Lagrangian array of points, which do not necessarily coincide with the underlying uniform Eulerian mesh points of the fluid computation. The interaction between the fibres and the fluid is handled by a smoothed approximation to the three-dimensional four point Dirac delta

DOI: 10.1002/cnm

function used to interpolate the fluid velocity to the solid and to apply the solid force to the fluid [33]:

$$\delta_h = \frac{1}{h^3}\varphi\left(\frac{x}{h}\right)\varphi\left(\frac{y}{h}\right)\varphi\left(\frac{z}{h}\right) \tag{5}$$

where h is the Euclid grid size, and

$$\varphi(r) = \begin{cases} \dfrac{3-2|r|+\sqrt{1+4|r|-4r^2}}{8}, & |r| \leqslant 1, \\ \dfrac{5-2|r|-\sqrt{7+12|r|-4r^2}}{8}, & 1 \leqslant |r| \leqslant 2, \\ 0, & 2 \leqslant |r|, \end{cases} \qquad r = \frac{x_i}{h} \tag{6}$$

The regulated delta function has compact support, and ensures that the force is conserved when it is spread to the Cartesian grid from the curvilinear mesh, and that the interpolation operator generated by δ_h is second-order accurate when interpolating the smooth functions [33].

Using the finite difference scheme with first-order upwind scheme as described by Peskin and McQueen [35], the matrix equation of the discretized Navier–Stokes equations (3) is derived as

$$KU^{n+1} = F(U^n) \tag{7}$$

where K is the stiffness matrix, F is the force vector, and U^n is the solution vector at the nth time step. As this is linear in U^{n+1} over a uniform Eulerian grid, the matrix can be solved using the Fast Fourier Transform method [35], provided that the boundary condition is periodic.

2.2. The MV model

Wheatley [36] has designed a MV prosthesis whose geometry is similar to that of the native MV, i.e. it has a larger anterior leaflet and a smaller posterior leaflet; see Figure 1(a). It is made of a polyurethane material and the prosthesis incorporates chordae, which originate from the valve annulus and traverse each leaflet, exiting at the leaflet edges to attach to the papillary muscle regions of the ventricle. There are 14 chordae in total, 8 in the posterior leaflet and 6 in the anterior leaflet. The valve is housed on a rigid D-shaped annulus, which attaches to the LV. The geometry of the MV is generated using the software SOLIDWORKS, and for the IB simulation it is represented as a surface constructed from one-dimensional elastic fibre segments, see Figure 1(b). More detailed methodology for the MV generation can be found in Watton *et al.* [22, 23].

The chordae have a cross-sectional area of $0.4\,\text{mm}^2$ and Young's modulus of 30 MPa. The leaflets have a mean thickness of 0.125 mm, and are modelled as a linear material with a Young's modulus of 5.4 MPa. As we used the designed MV, which is made with polyurethane material, the true anisotropic property of the native valve cannot be matched. However, some degree of this anisotropic behaviour is included by the chordae that are imbedded within the valve leaflets. Note that for the polyurethane material, the incremental stiffness decreases slowly as a function of stretch. Hence, over the small range of stretches the valve leaflets experience it seems a reasonable approximation to assume a constant stiffness (equal to the maximum initial stiffness). The valve leaflets also vary slightly in thickness; this was ignored and a uniform thickness distribution was

DOI: 10.1002/cnm

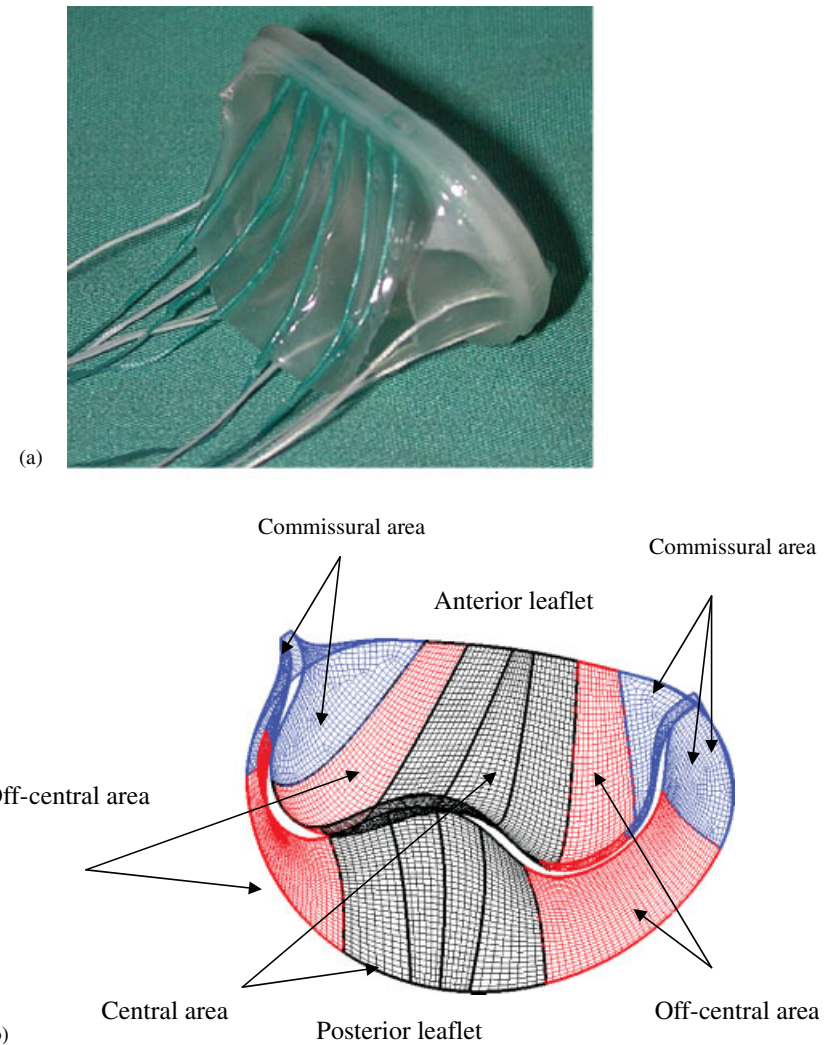

Figure 1. (a) The designed MV prosthesis with chordae (D.J. Wheatley 2002, Mitral valve prosthesis Patent no. WO03037227) and (b) the meshed MV model with posterior and anterior leaflets, and is divided into central, off central and commissural areas.

modelled. These approximations were tested and deemed to be acceptable for the range of pressure we studied [22].

Following Watton *et al.* [22], we generated the MV model from the IGES file of the designed valve, which was imported to Gambit to create quadrilateral finite element mesh. The nodal coordinate data and the connectivity are then used to create the IB fibre model. For the anterior leaflet, 3718 elements are used to generate 22 308 fibre ends, and for the posterior leaflet, 4269 elements are used, leading to 25 614 fibre ends. The requirement for the fibre grid is that the minimum grid density should be at least twice as much as the fluid grid.

DOI: 10.1002/cnm

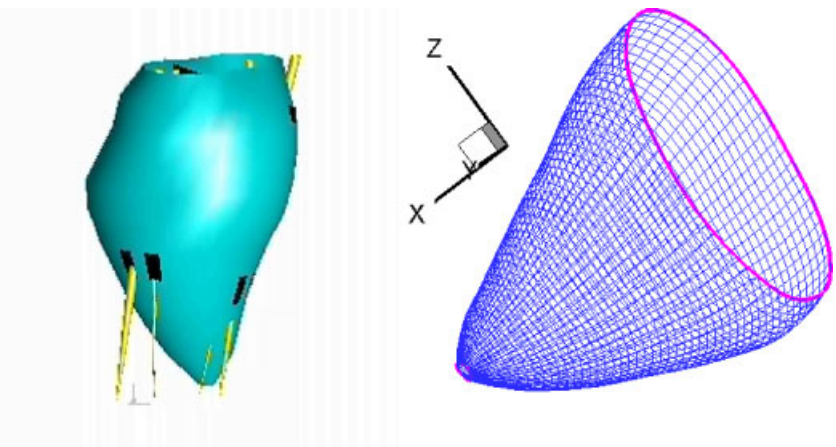

Figure 2. The LV model built from MRI data of a health human subject. The two chordae attachment point s (CAPs) are estimated from the LV motion, in the same way as used by Watton *et al.* [23].

2.3. The LV model

The imaging software CMRTOOLS (www.cmrtools.com, Imperial College, U.K.) is used to analyse high-resolution MRI data of the dynamic motion of the ventricle (32 phases per cardiac cycle of about 0.75 s) from a healthy subject. This software enables the user to interactively define the geometry of the ventricle and the directional axes of the papillary muscles at each time step. From the intersection of these coordinate data sets, the papillary muscle regions of the ventricle can be identified, see Figure 2(a).

The geometry data for the ventricle, the papillary muscle axes, and the mitral annulus are imported into the Fortran subroutines to generate the mesh of the LV and motion of CAPs. For the purpose of the computational simulations, it is convenient to use the mitral annulus as a fixed reference frame. Consequently, a coordination transformation is required in the subroutines to define the motion of the LV relative to that of the mitral annulus.

The MRI data of the LV are obtained from 48 equal distance scanning at every time step. With the LV contraction, the nodes obtained at different time step are not necessarily the same material points. Therefore, in order to estimate the LV motion, the material points of the LV are tracked according to their distances between the LV apex and the mitral annulus point. The mesh of the LV based on these material points is then refined for the IB simulation to prevent the fluid leakage. Stiff tethering fibres are attached to all nodal fibre points of the model. The dynamic motion of the LV is then controlled by prescribing the geometrical motion of these tethering points. Figure 2(b) illustrates the mesh of the LV at a time instant. In the LV model, 48 195 quadrilateral elements with 48 384 nodes are used to generate the fibre mesh, which gives rise to 96 957 fibre ends for the IB simulation.

2.4. The chordae attachment points (CAPs)

Once the papillary muscle regions of the ventricle are identified, the 14 chordae are split into two groups that are attached to the papillary muscle regions of the ventricle. The time-dependent

DOI: 10.1002/cnm

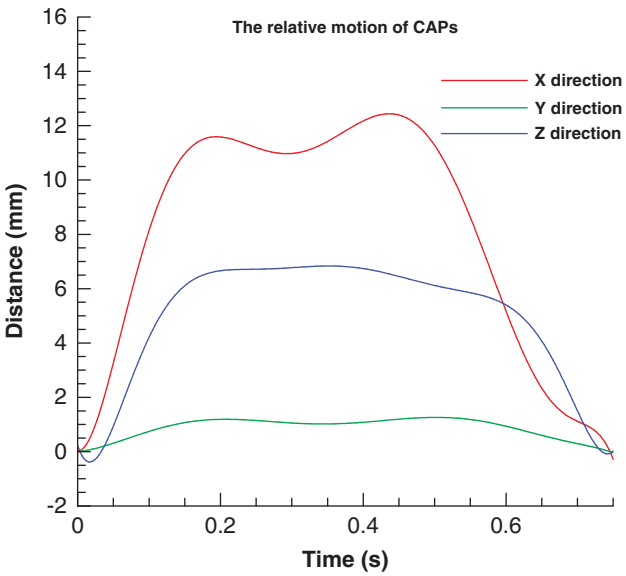

Figure 3. The relative movement of the CAPs with time.

motions of these CAPs are obtained from the corresponding regions of the LV, shown in Figure 3. Note that Watton *et al.* [23] only considered the longitudinal motion of the CAPs; however, in this paper the CAPs are allowed to move in all three directions to follow the LV motion. This is because while the longitudinal motion of the CAPs is the greatest, the two lateral motions are not negligible, i.e. they can be as much as 50% of the longitudinal motion, see Figure 3.

Papillary muscle contraction is not modelled explicitly in this study. However, to simulate its effect, we consider a special case, in which the spatial locations of the CAPs are fixed (relative to the mitral annulus). This simulates a physiological scenario in which the papillary muscles are functioning in such a way that during LV diastole, they relax to cancel out the dynamic motion between the mitral annulus and the papillary muscle regions of the ventricle. In reality, the papillary muscles' function may not be able to fully compensate for the LV motion. In fact, their exact function is still of much debate [37–42]. However, our model with these two extreme cases will provide us with a range of behaviours that mimic a physiological situation. In addition, a corresponding Tube model is also considered in order to assess the effects of the vortex flow within the LV.

2.5. Dynamic IB simulations

The MV model is placed into the fluid domain for the IB simulation. The fluid domain is chosen to be 0.16 m long and 0.16 m wide with a $64 \times 64 \times 64$ grid. A guiding tube and an additional circular plane are constructed from a mesh of fibres to enlarge the initial valve housing. These help to mount the MV onto the LV model to ensure that all the incoming fluid is directed into the LV without any side leakage. Stiff tethering fibres are attached to all nodal fibre points of the tube, the plane, and valve housing to render these regions effectively rigid. Figure 4 illustrates how the

DOI: 10.1002/cnm

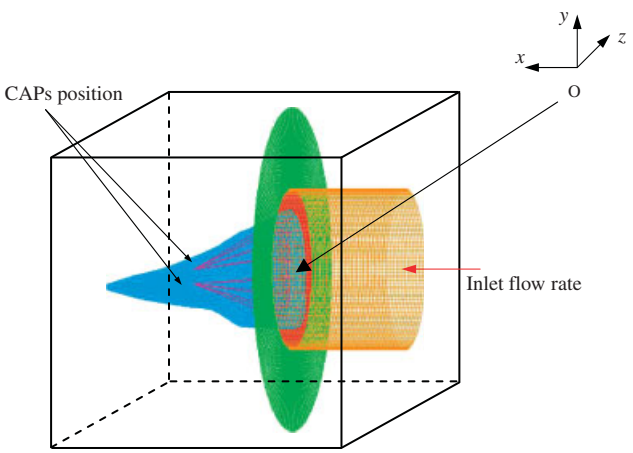

Figure 4. The whole computational model, with the fluid box of size $0.16*0.16*0.16\,\mathrm{m}^3$. The MV is fitted at $x=0.04\,\mathrm{m}$ from the flow inlet plane (right), and the origin of the coordinates O is chosen to be at the centre of the MV annulus plane.

MV model is fitted with the LV model. For the Tube model, the settings are the same as in the LV model, except that the guiding tube is extended to the whole domain to replace the LV.

A periodic velocity profile based on a pulsatile flow rate is exerted on the input fluid of the fluid domain. The pulsatile flow rate has to be calculated according to the change of the volume of the LV due to mass conservation. This makes the current simulation essentially different from our earlier work in which the flow rate is prescribed from measurements taken from an experimental test rig [23]. In the current case, the peak flow rate appears to be much higher, and the waveform is also different. This may be due to the inaccuracies of the LV motion extraction from MRI (as the exact material planes could not be extracted), or it could reflect the specific subject used.

The LV volume change with time estimated from the MRI images is shown in Figure 5, together with the corresponding flow rate. These curves are representative of a general human LV [43]. In these simulations, $t=0$ denotes the beginning of the ventricle diastole. The flow rate reduces to zero around 0.5 s and the pressure inside the LV reaches its maximum systolic pressure. The flow rate becomes negative as the valve is closing. This is the closing volume, caused by the movement of the MV leaflets during closing [44]. After the MV is closed, the aortic valve is then opened. As the aortic valve is not considered in the model, the simulation can only include a part of the cardiac cycle, from the MV opening to the end of diastole, i.e. from 0–0.5 s.

Three simulation models are considered: (i) the LV model: MV inserted in LV with chordae attachments points embedded in the wall of the ventricle; (ii) the LV Fixed-CAP model: MV inserted in LV with fixed CAPs relative to mitral annulus; (iii) the Tube model: MV inserted in a tube with dynamic CAPs—with same relative motion as in (i).

A fixed time step is chosen to be 0.25×10^{-4} s; therefore, a total of 20 000 steps were required for each cardiac cycle (0–0.5 s), which took about 35 h on a Dell Precision T5400 Workstation with 16 GB DDR2 667 Quad Channel FBD Memory and 2330 MHz. TECPLOT software was used for graphical post-processing.

DOI: 10.1002/cnm

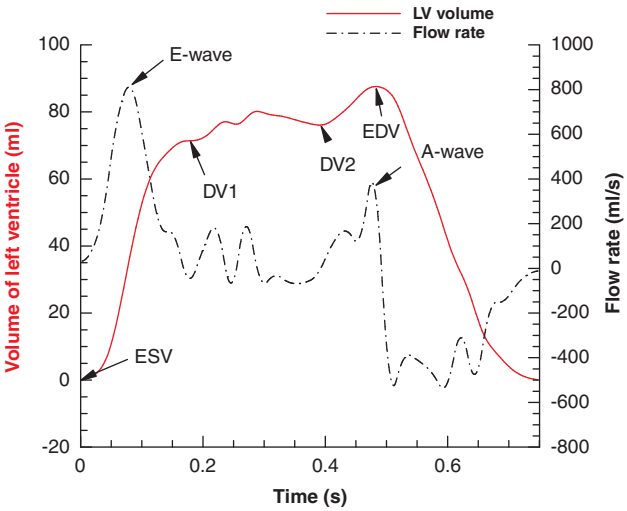

Figure 5. The change of the measured volume of the left ventricle from MRI data with time (solid) and the estimated flow rate through the mitral valve with time (dash-dot). This flow rate is used as the inlet boundary condition for all three models investigated. The corresponding events are marked as the end-diastole volume (EDV), end-systole-volume (ESV), the end of the early rapid filling period (DV1), and the start of the second peak (DV2). The times of these events agree with *in vivo* measurements by Hammermeiser and Warbasse [43]. The corresponding flow rate has two major peaks, A-wave, which indicate the early rapid filling peak, and the E-wave, given by the atrial contraction. Note that small waves in the volume data are amplified in the corresponding flow rate.

3. RESULT

In the following, we will focus on the LV model. However, results will be compared with the other two models: the LV Fixed CAP and the Tube models.

3.1. The flow field

To see the three-dimensional flow field generated by the LV motion, we present the flow velocity vector plots of the LV model on the y- and z-planes in the middle of the MV for every 0.05 s, see Figure 6. For comparison, results of the Tube model are shown in Figure 7. The flow patterns for the LV and the LV Fixed-CAP models are quite similar, hence results of the latter case are not shown.

It is observed that flow field of the LV model is significantly different to that of the Tube model. In the Tube model (Figure 7), the main feature of the flow is a forward jet in the longitudinal direction, which is extended further downstream. In the y-plane, there are not distinct vortices, though at $t=0.1$, there is a small vortex attached to the posterior leaflet; then between $t=0.25$ to 0.4 s, a large anti-clock-wise vortex is observed stretching from the posterior leaflet to the outlet boundary. In the z-plane, the forward jet formed at $t=0.1$ s is immediately accompanied by two vortices at each side, though their location is not entirely axis-symmetric, with a slightly larger one on the anterior side. The vortices persisted until $t=0.35$ s, long after the jet disappeared at $t=0.2$ s. However, in the LV model, the flow is more complicated. In the y-plane, the flow formed

DOI: 10.1002/cnm

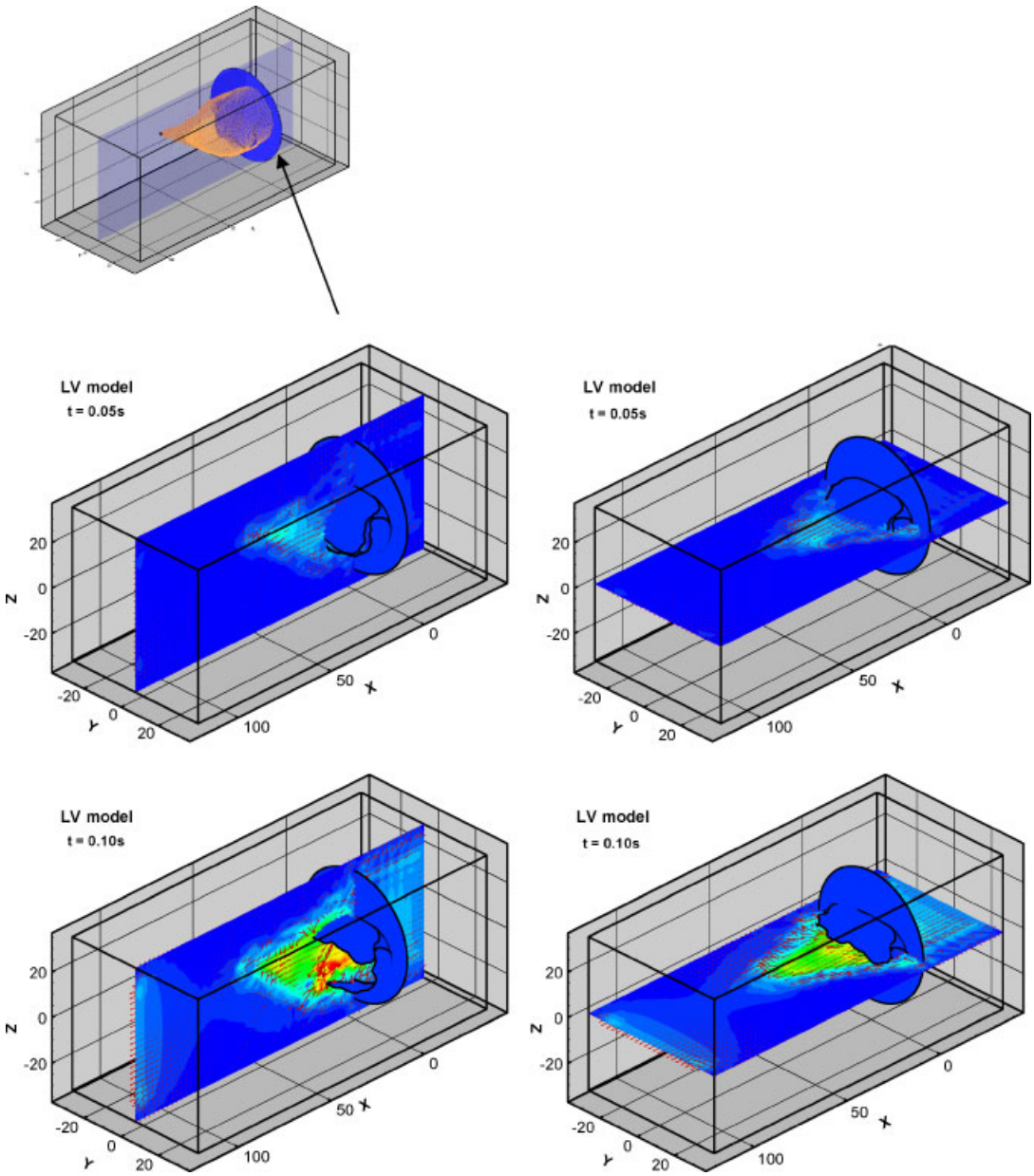

Figure 6. Velocity vector plots of the LV model at very 0.05 s between 0–0.5 s: (a) for z-plane ($y=0$) and (b) y-plane ($z=0$). Note although the moving LV is included in the simulation, as indicated by the insert (at $t=0$), it is not plotted for graphic clarity. The unit shown in the coordinate axes is in mm.

its strongest jet slightly later than that in the Tube model, i.e. at about $t=0.15$ s; presumably due to a stronger resistance of the LV wall. The jet then hits the LV wall, and is forced to bend downwards and around the LV wall enclosure. There is a clear clockwise vortex formed at $t=0.2$ s

DOI: 10.1002/cnm

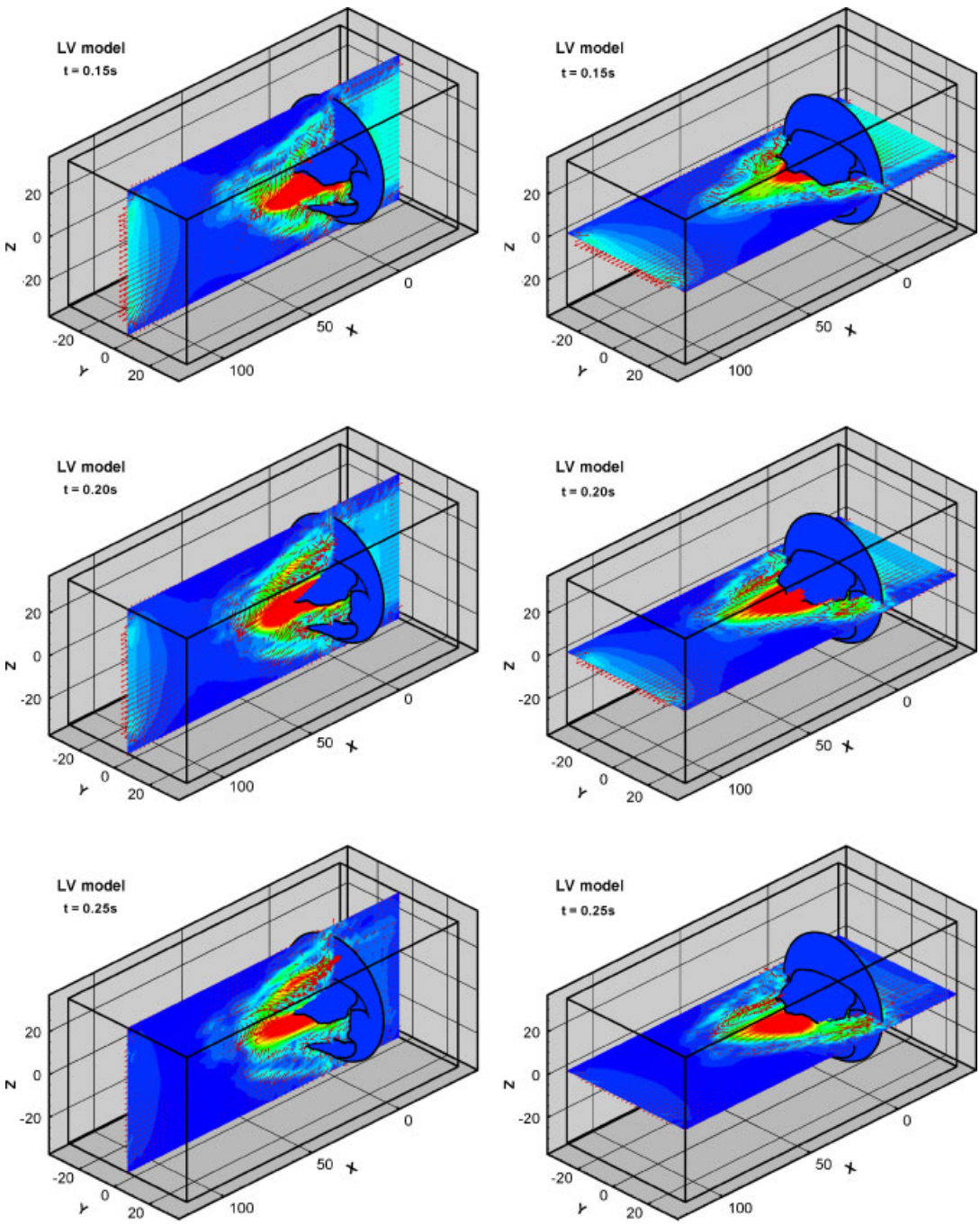

Figure 6. *Continued.*

DOI: 10.1002/cnm

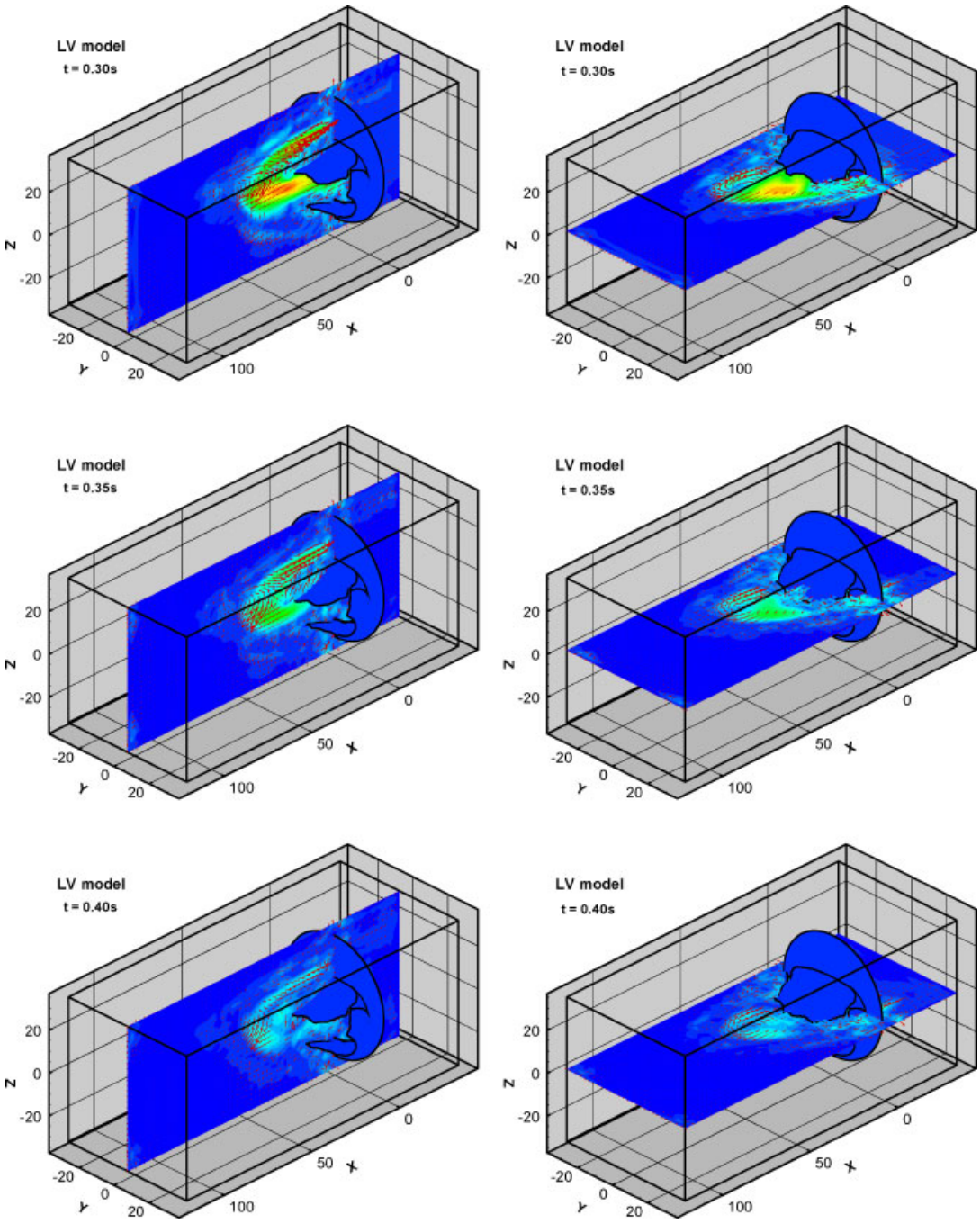

Figure 6. *Continued.*

DOI: 10.1002/cnm

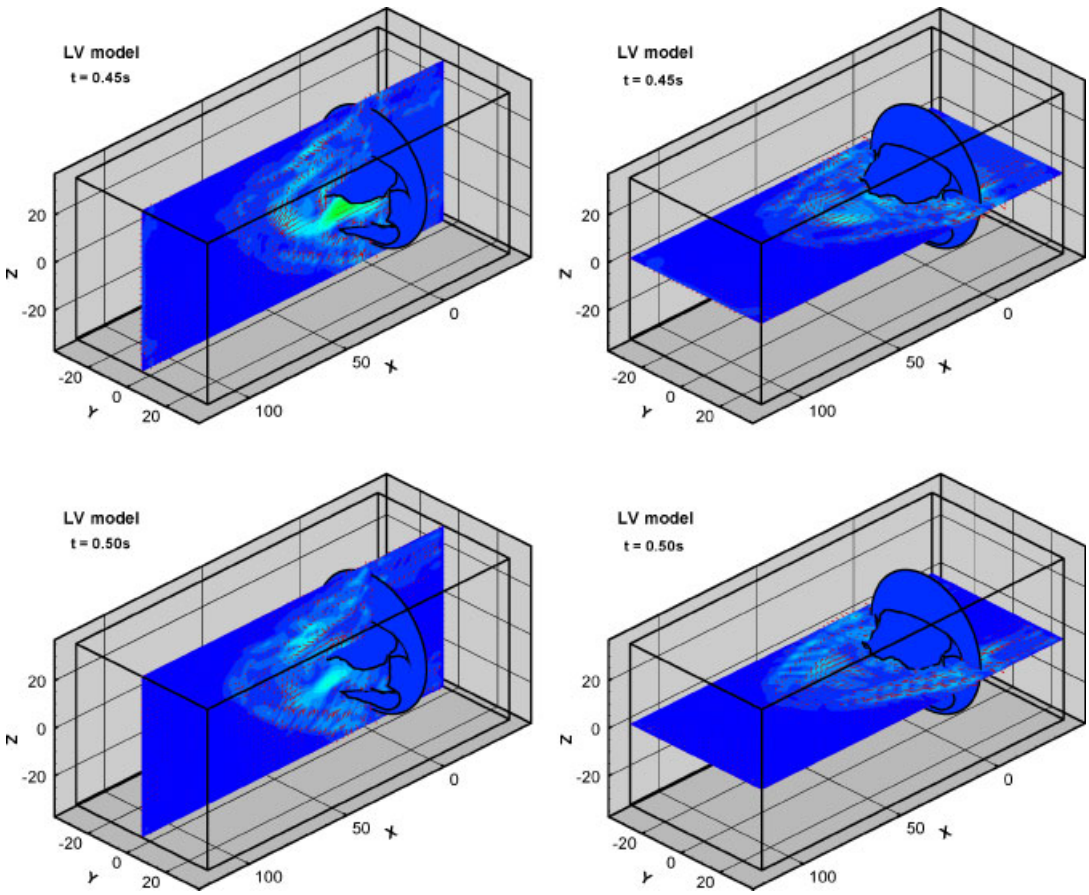

Figure 6. *Continued.*

at the anterior side, which is shed downstream towards the LV apex, and disappears at $t = 0.3$ s. The flow pattern is highly disturbed at the posterior side; however, no single vortex is detected there. On the z-plane, two vortices, both at the same side, one anti-clockwise and one clockwise, are seen with the forward jet at $t = 0.15$ s. These, however, merged into one large clock-wise vortex at $t = 0.25$ s, eventually occupying the middle section of the plane and persisting throughout the rest of the diastole. Again, the flow is more disorganized near the posterior leaflet, especially around the commissural area. The flow calms down temporarily between 0.35–0.45 s; then with the secondary acceleration near $t = 0.45$ s as the atria is contracted (see Figure 5), a much weaker vortex then appears near the anterior leaflet edge in the y-plane.

The flow field of the LV Fixed-CAP model (not shown) is qualitatively similar to that of the LV model. The only difference seems to be that the leaflet opening is more asymmetric due to the lack of the chordae pulling, since in this case the leaflets, which have no bending stiffness, are under strong influence of the highly asymmetric flow around them.

DOI: 10.1002/cnm

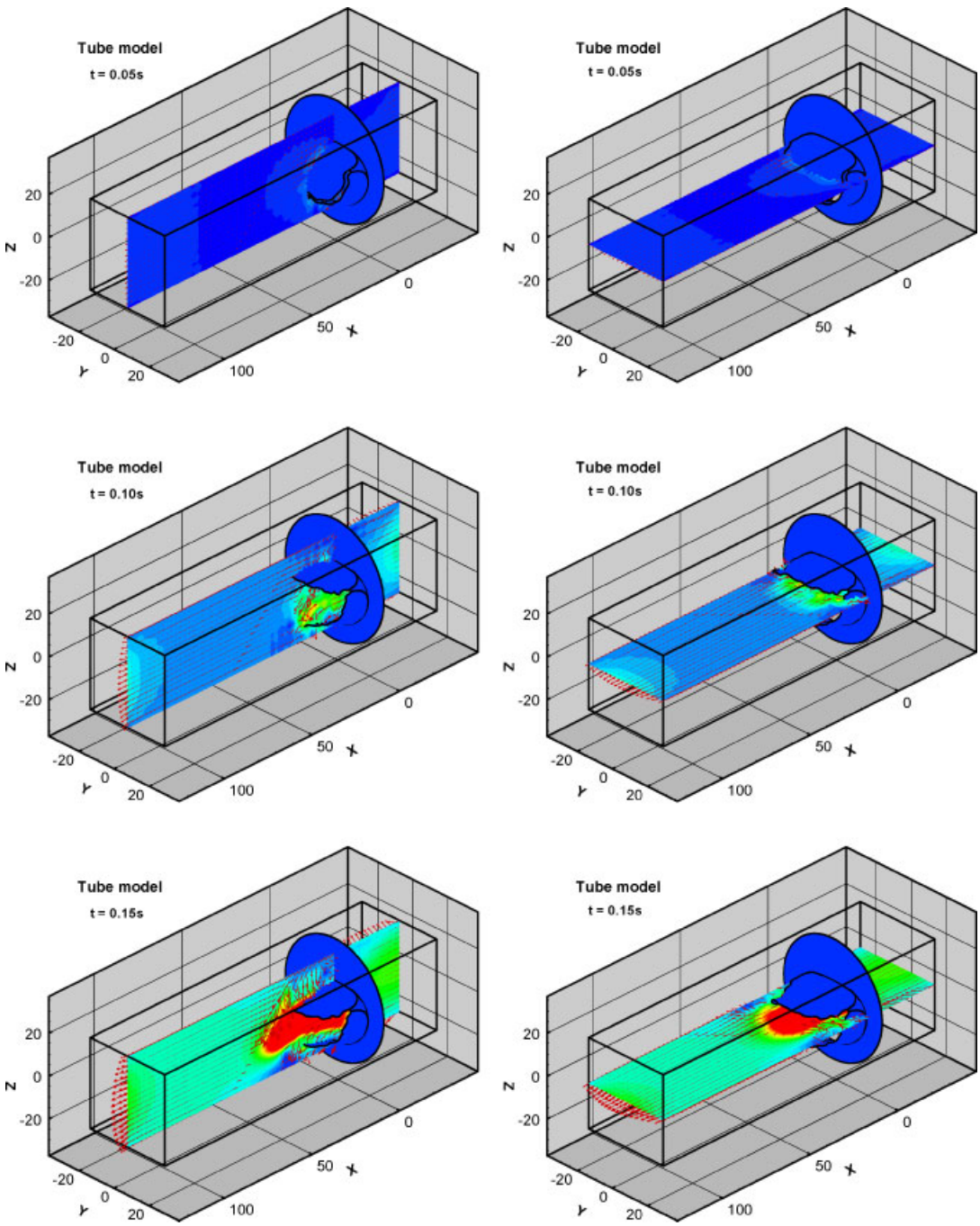

Figure 7. Velocity vector plots of the Tube model at every 0.05 s between 0–0.5 s, for (a) z-plane ($y=0$) and (b) y-plane ($z=0$). The unit shown in the coordinate axes is in mm.

DOI: 10.1002/cnm

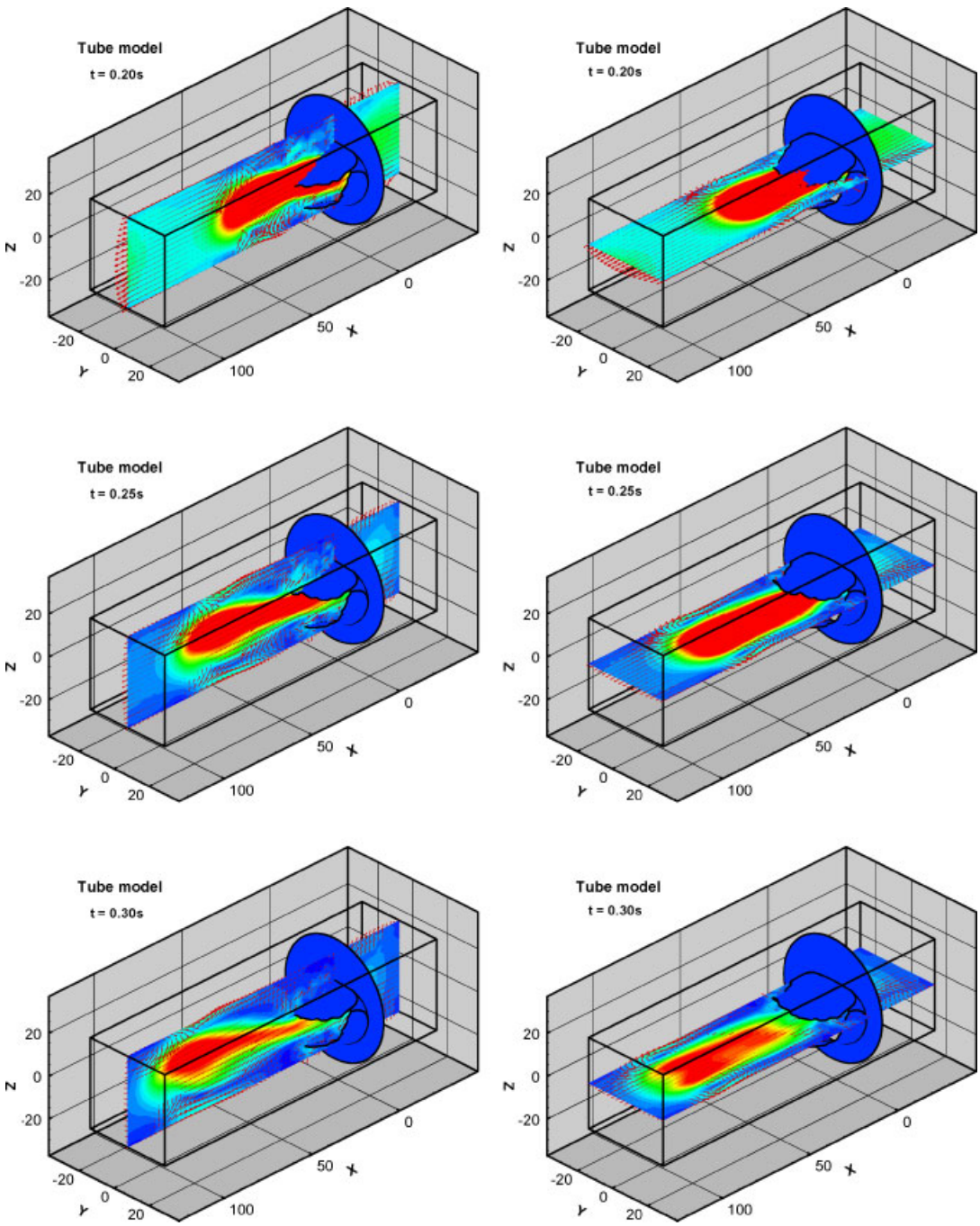

Figure 7. *Continued.*

DOI: 10.1002/cnm

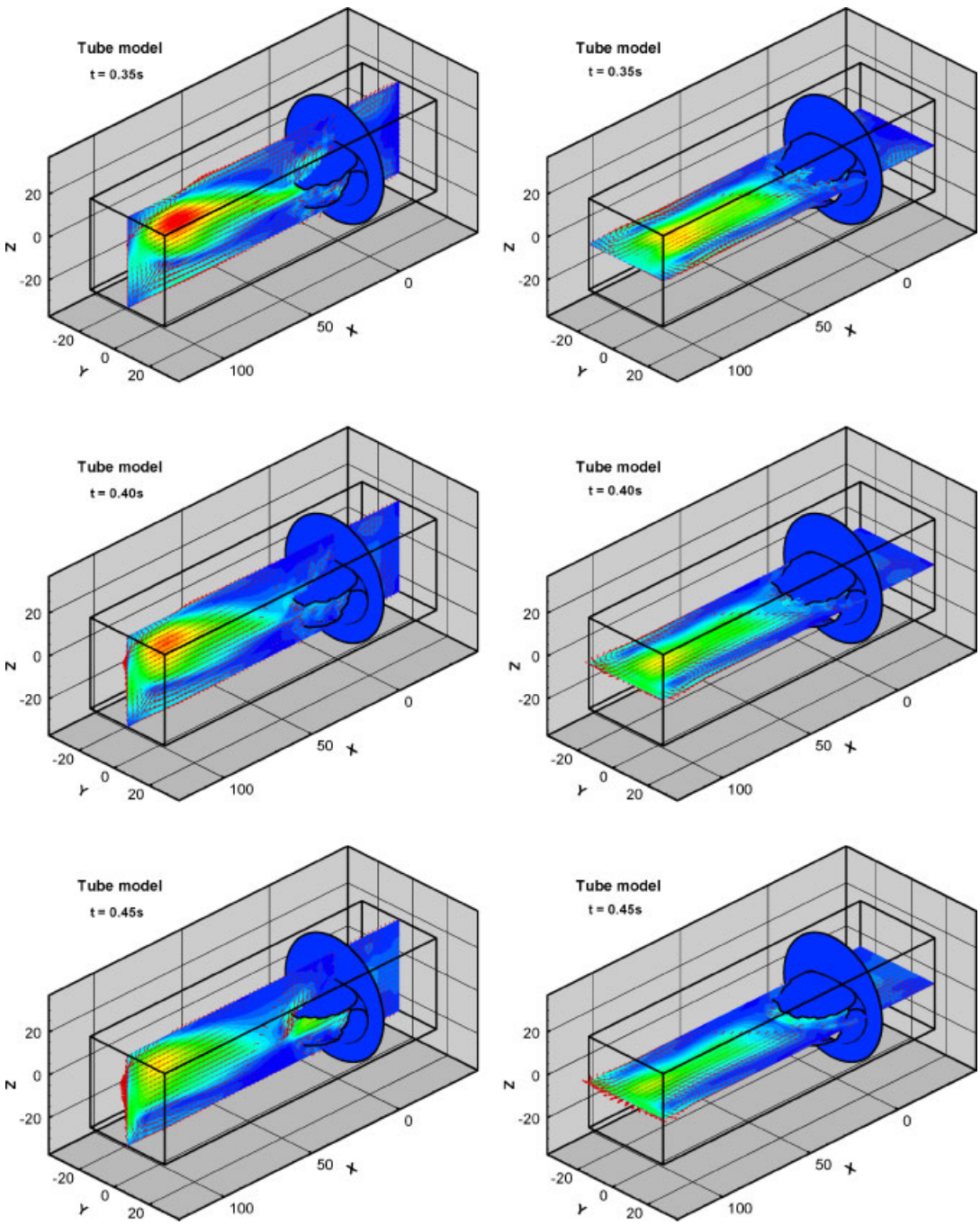

Figure 7. *Continued.*

DOI: 10.1002/cnm

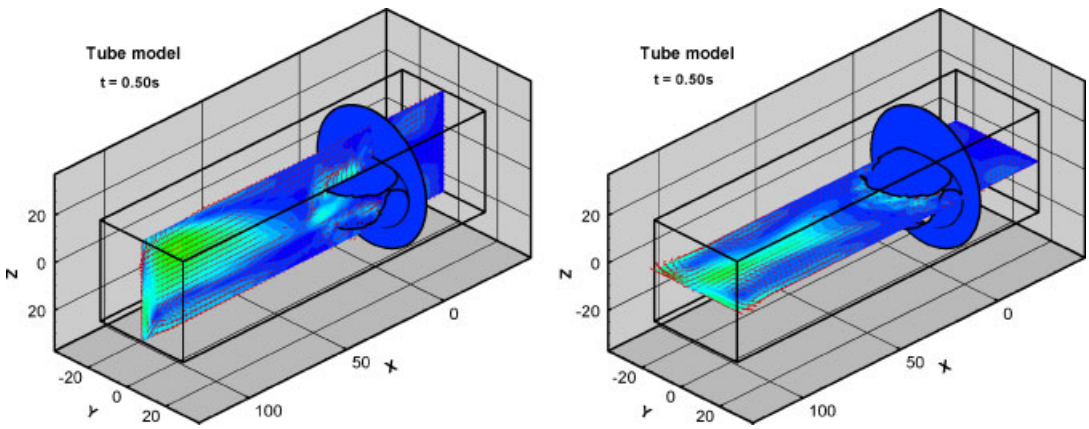

Figure 7. *Continued.*

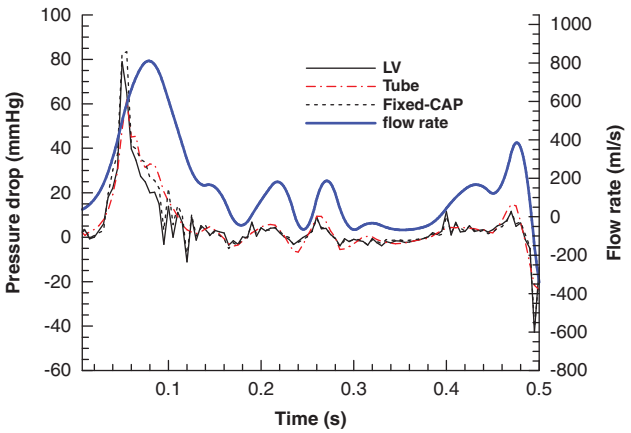

Figure 8. The pressure gradient history across the prosthesis MV of the three models, calculated between 2.5 cm upstream and 2.5 cm downstream. The flow rate curve is also overlapped to show the correspondence events.

Although the MV should be fully closed after 0.5 s, in all cases considered the MV remains open.

3.2. Pressure gradient across the prosthesis

The pressure gradients across the prosthesis (measured at 2.5 cm upstream and 2.5 cm downstream of MV) of the three models are shown in Figure 8. The corresponding flow rate curve is also shown. Between $t = 0$ and 0.05, flow is pushing onto the still closed valve, and the pressure gradient starts to build up. Then at $t = 0.05$ s, the valve opens and the LV is relaxing back. The immediate valve opening to the flow causes the first drop in the pressure gradient. Then the flow rate reaches its peak (E-wave) and the rapid filling phase is ended. With the deceleration of the flow rate, the

DOI: 10.1002/cnm

pressure gradient is dropped to zero level, and as the flow is highly unstable with vortices, there are observable oscillations in the pressure drop; similar oscillations are observed from *in vitro* experiments [38]. Other peaks of pressure drop are synchronized with the waves of the flow rate. It is interesting to note that the pressure drop across the valve is highest in the LV Fixed-CAP model and lowest in the Tube model. Since the only difference between these models is the flow condition, the increase in the opening pressure gradient must be a consequence of the LV motion and the vortex flow induced. In other words, the presence of the LV wall and the complex pattern of the dynamic flow provided stronger resistance to the opening pressure. Surprisingly, the opening pressure gradient of the LV Fixed-CAP model is only marginally higher than that of the LV model, suggesting that the chordae pulling plays a small role here. In the earlier MV model without LV attached, the CAPs motion was found to reduce the opening pressure gradient significantly [23]. Clearly, this is because the flow structure of the LV model has much more significant effect on the valve opening compared with the chordae pulling. The consistent finding is observed in the valve stretching, to be shown in the following. The two pressure drop peaks presented in the LV and the LV Fixed-CAP models just prior to the valve opening are the direct result of the interaction of the LV base and the impinging flow, as we discussed in Section 3.1. It is noted that the valve opening time in the Tube model is slightly delayed (at about $t = 0.055$ s) compared with the LV models.

The pressure drop history curves in the LV and the LV Fixed-CAP models have more oscillations than that in the Tube model. This may be partly attributed to the complicated flow swirling inside the LV, and partly due to the fact that our LV model is not smoothed in space over time (though linear time interpolation is used to allow smaller time steps); thus, the LV is accurate only at the 32 snaps of time recorded from MRI. This will affect the pressure more acutely due to the incompressibility condition, although this effect has been somewhat reduced by allowing the LV to be slightly compliant.

3.3. The stretch of the chordae

The variations of the stretch with time in the anterior and posterior chordae of the three models are shown in Figure 9(a)–(c). We can see that in all three models, the anterior chordae are not under tension, and hence we will not discuss these further. All the posterior chordae are taut during opening. The chordae stretch of the LV Fixed-CAP model is the smallest of the three models, i.e. the average stretch is 1.1. This is to be expected, since in the LV Fixed-CAP model, the chordae stretching is caused entirely by the forward flow. The stretch of the chordae in the LV model is the highest, of the order 1.25, as these chordae are pulled by the forward flow as well as the CAPs. The asymmetric feature of the flow also makes the chordae stretch slightly differently depending on their locations compared with that of the Tube model.

3.4. Average stretches within the leaflets

The average stretches (over a section of the surface) during the dynamic cycle of the leaflets of the three models are illustrated in Figure 10(a)–(j). The averaged stretches are shown for three regions of the anterior and posterior leaflets: namely, central, off-central and commissural regions of the leaflets. In the central and off-central regions, both longitudinal (following the direction of chordae) and circumferential stretches are plotted. In the commissural regions of the leaflets, the surface average of the maximum fibre stretch in each element is shown. The results for off-central

DOI: 10.1002/cnm

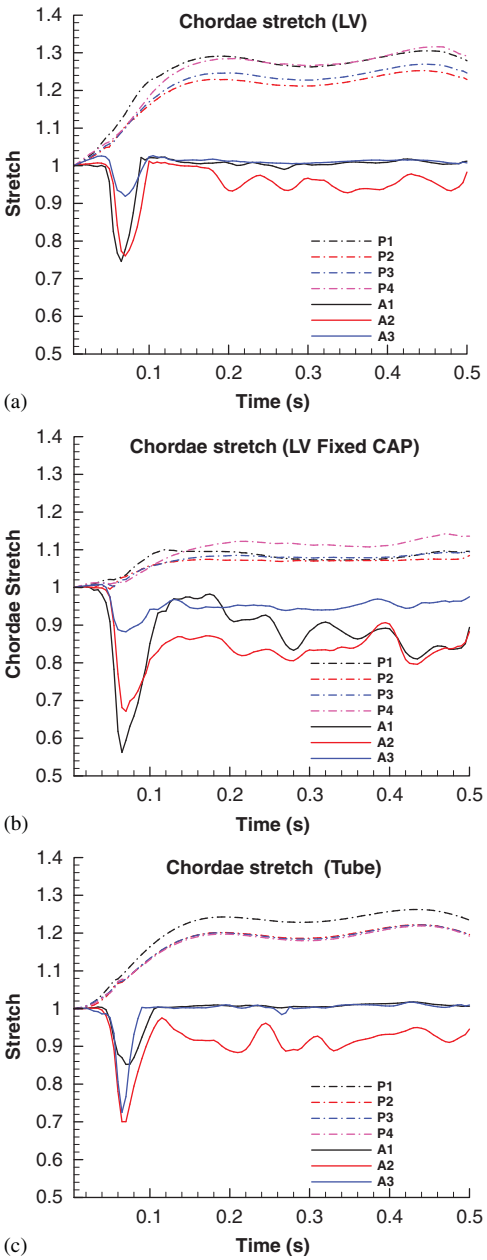

Figure 9. The variations of stretch with time in the anterior and posterior chordae of the LV model (a); the LV Fixed-CAP model (b); and the Tube model (c).

DOI: 10.1002/cnm

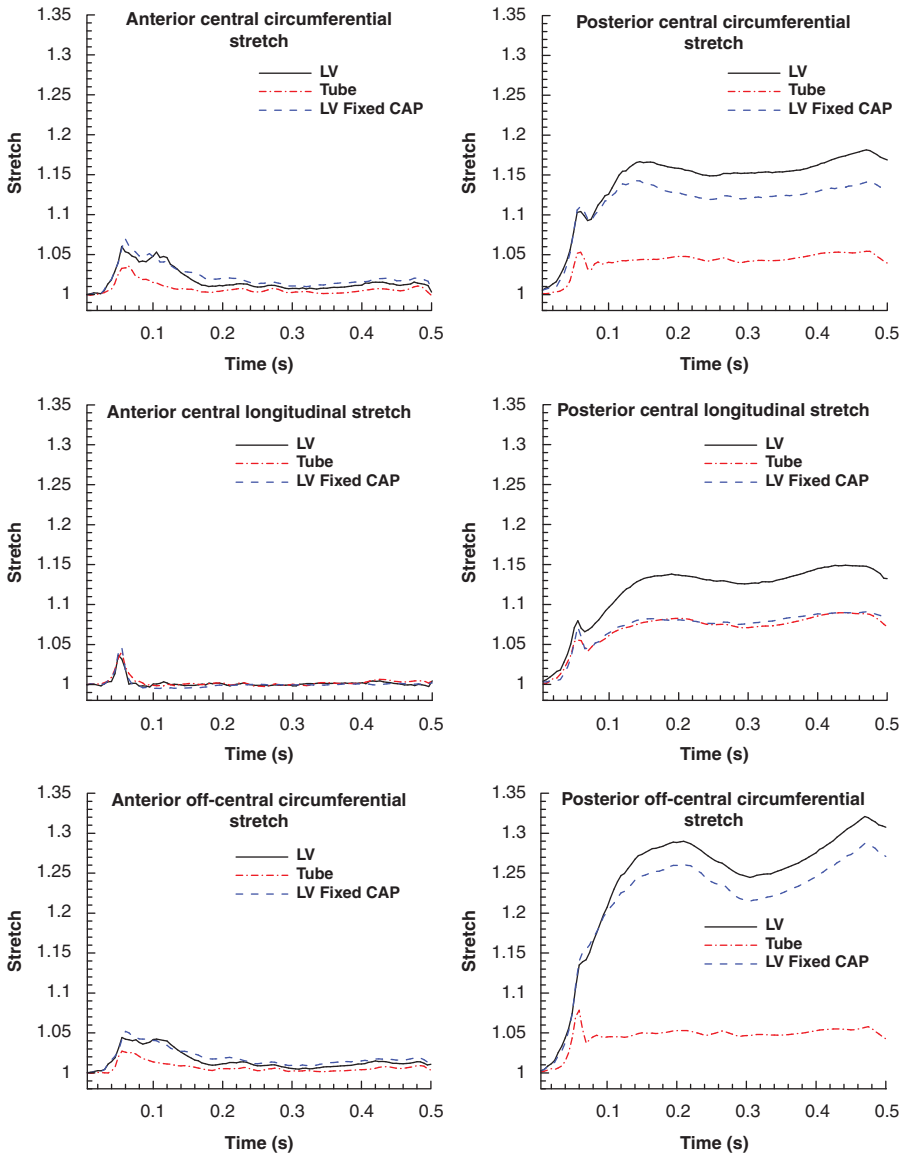

Figure 10. The averaged circumferential and longitudinal stretches of anterior and posterior leaflets in different areas, as marked in Figure 2(a).

areas are similar to those of central areas except that the differences between longitudinal and circumferential directions are not so distinct compared with the central regions.

Figure 10 illustrates that in the longitudinal direction, all three models predict similar stretch magnitudes. However, the two LV models experience higher stretch in the circumferential direction compared with that of the Tube model. This is consistent with the pressure gradient presented

DOI: 10.1002/cnm

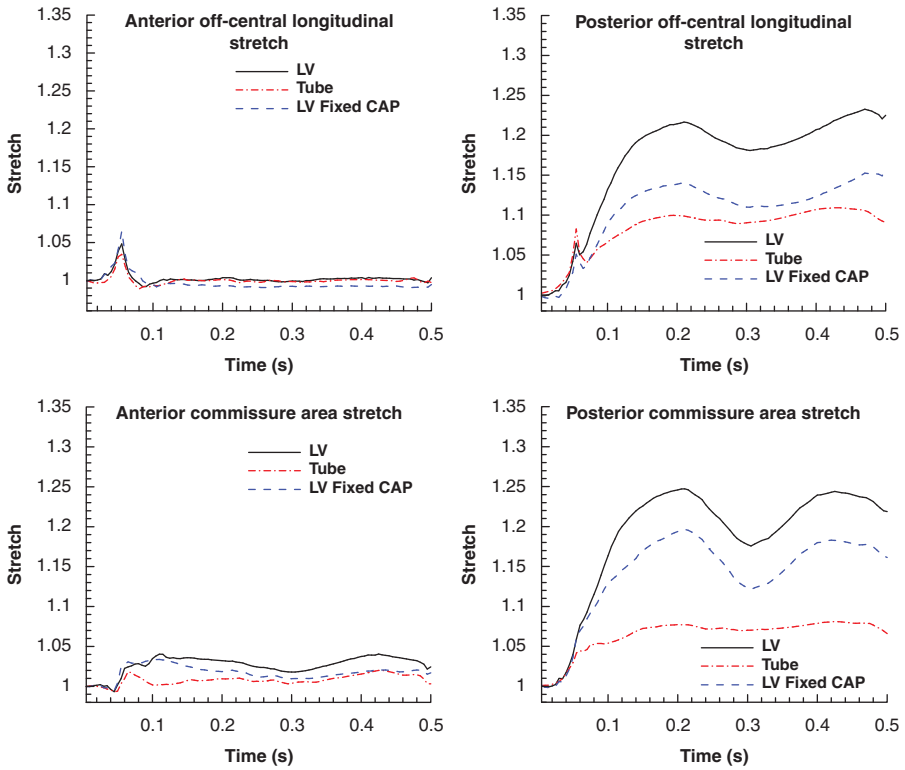

Figure 10. *Continued.*

earlier. Similar behaviour is observed in the commissural region, and the LV model demonstrates the highest stretch. Note that in Figure 10, the differences of the anterior leaflet stretch between the three models are much smaller, and in most cases similar to the posterior leaflet stretch. Therefore, in the following, we will focus on discussing the posterior leaflet stretch.

For the posterior leaflet, the average stretch in all regions is much higher than the anterior leaflet. This feature was previously observed by Watton *et al.* [23]. However, in the longitudinal direction, the first peak of the stretch prior to opening is significantly lower compared with the follow on stretch after the valve is fully opened and the flow jet has disappeared. It is also noted that with the LV models, the circumferential stretch is greater than the longitudinal one, while in the Tube model, the longitudinal stretch is greater. This again highlights the strength of the flow vortex inside the ventricle. In addition, the maximum stretch of the LV models occurs in the commissural area where the flow is most complicated, while the maximum stretch of the Tube model occurs in the longitudinal direction. A second peak of stretch is also exhibited in the LV models, which are closely associated with the jets and the subsequent vortices formed in the LV during the two major peaks of the flow rate, just before 0.1 and 0.45 s, respectively.

Compared with the LV Fixed-CAP model, the LV model has higher stretch due to the chordae pulling. Therefore, if the papillary muscles were in place and could indeed compensate the CAP motion, then the MV posterior leaflet will not be so stretched, especially in the commissural area.

DOI: 10.1002/cnm

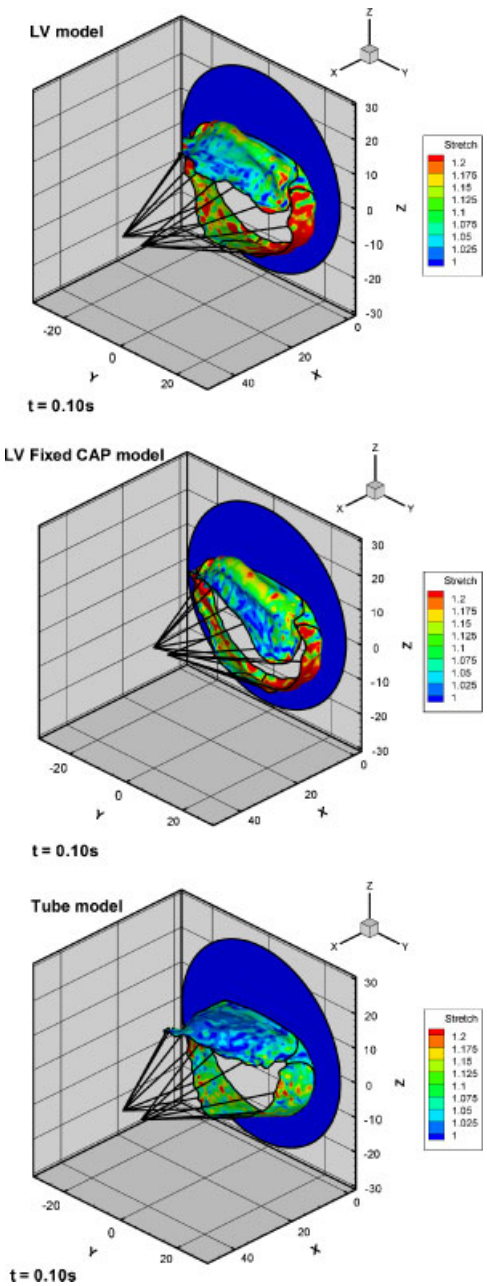

Figure 11. The stretch of the three models at the fully opened state at $t = 0.1$ s.

3.5. Three-dimensional view of the valve stretch

To present a clearer picture, the three-dimensional stretch of the three models at $t = 0.1$ s is shown in Figure 11. This picture shows that the maximum stretch of the Tube model occurs around the

DOI: 10.1002/cnm

chordae insertion positions inside the leaflets; therefore, this stretch is mainly due to the chordae pulling. However, the maximum stretch of the two LV models occurs at the commissural regions where the flow is highly complicated.

4. DISCUSSION

In this paper, the effect of the vortex flow induced by the LV contraction on a prosthetic MV dynamics has been studied. Three models are considered, the LV, the LV Fixed CAP, and the Tube models. The most striking difference between the LV models and the Tube model is the presence of the large clockwise anterior vortex in the LV, which is absent in the Tube model. Previous research has indicated that dynamics of the cardiac LV during diastolic filling play a critical role in dictating overall cardiac health [45]. The flow vortex presented here is similar to previous observations [24, 25], although due to the lack of the aortic valve in place, only diastole phase of the cardiac cycle has been investigated. At the early rapid filling phase, the flow is featured by a strong jet, which impinges on the LV wall and swirls around in a clockwise fashion, forming a main clockwise vortex. This vortex persists through the remaining of the diastole phase. These observations agreed, to some extent, to what Long *et al.* [30] observed in their LV flow. However, unlike what Long *et al.* [30] discovered, the jet flow is not accompanied by two vortices located on both sides of the jet, rather a large vortex appeared in the large anterior leaflet side, and a much smaller and short-lived vortex in the posterior side. This is because Long *et al.* [30] did not have MV attached in their model; therefore, the flow inside LV is not affected by the presence of the MV. Long *et al.* [30] also observed anti-clockwise vortex in the three cases they studied and clock-wise vortex in one case. Here, the flow pattern only presented a clock-wise vortex. The reason for this is not clear as we only studied one MRI LV model. It is thought that this could be due to the shape and motion of the LV recorded for different subjects.

The impact of the LV motion and the vortex flow to the MV dynamics is highly important. The LV models clearly show a greatly increased stretch in the valve compared with that of the Tube model. The effect of pulling of the chordae due to (or lack of) the papillary muscle extension is also significant, especially for the chordae and posterior leaflet; however, the difference between the LV model and the LV Fixed-CAP model is smaller than that from any one of them to the Tube model.

Although the MV should be fully closed after 0.5 s, in all cases considered the MV remains open. Similar behaviour was observed by Watton *et al.* [23] in their Tube model (an artificial pressure gradient was needed to force the valve to close in the simulations). This is due to an inherent limitation of the modelling that the bending resistance of the valve and chordae is not currently modelled. In fact, in a recent simulation using the adaptive mesh IB methods (IBAMR), it is found that with local mesh refinement and chordae bending stiffness, the MV closes effectively at $t = 0.5$ [46]. As the MV cannot close properly in this simulation, contact problem does not occur. Even if the MV can close properly, contacts cannot be effectively dealt with using the current approach. This is because contacts happen when the systolic pressure is applied and the flow rate is zero. Therefore, using flow rate (as we do here) as the boundary condition, we cannot reproduce the systolic pressure drop (i.e. zero flow rate can occur under any pressure drop when a valve is closed). In order to simulate contact problem, the pressure drop boundary condition should be used. This is one limitation of the current model.

DOI: 10.1002/cnm

In the present paper the Tube model is used for comparison purpose. However, the Tube model here is different to the one used by Watton *et al.* [23] in two major aspects: (i) the flow rate in the present model was estimated from the MRI of the LV volume change while the previous study prescribed a flow rate obtained from an experimental rig; (ii) in this model, the CAP motion in all three spatial directions is considered, while the previous study only considered longitudinal motion.

For the two LV models, we utilize the specific LV motion; hence, the flow rate is fixed and there is no flexibility in adjusting it. In addition, by prescribing the flow rate and the LV motion, our simulations tend to produce extra oscillations in the pressure gradient field, which are enhanced by the fact that the LV wall modelled here is very stiff. Therefore, any small mismatch of the flow rate (estimated from the volume change) and the wall movement can cause the pressure drop to change rapidly due to the fluid incompressibility. This oscillation can be reduced if the LV wall is made self-contractive and the motion is not prescribed. A more accurate approach was used in the context of the active heart muscle mechanics by Peskin and McQueen [34]. However, the down side of this approach is its inhibitively high computational cost.

Although we have made an effort to improve our previous MV model by incorporating the LV motion, the IB method we used still suffers from the same shortcomings as we discussed in Watton *et al.* [22, 23]. Namely, the numerical scheme used is only of first order in time and space, the Eulerian mesh is uniform, and the bending stiffnesses of the chordae and valve leaflets are neglected. The structure grid spacing has been tested over several different grids, and the error between different Lagrangian grids is acceptable. However, it is noted that due to the uniform mesh used for the fluid domain, no significant grid improvement can be made within our available computational resources and time: the next finer fluid mesh that can be used needs to be $128 \times 128 \times 128$. In addition, it is well known that when the valve is in the closed state, the local fluid field is singular and it is almost impossible to resolve this perfectly (i.e. to make it grid independent). More specifically, due to the finite size of the delta function, the pressure required to open a completely closed valve will be infinite. Therefore, the magnitude of the peak opening pressure drop estimated in the simulations is probably significantly over-estimated. The peak of the pressure drop can be reduced as the fluid grid space is reduced. In fact, in order to open the valve in the immersed boundary model, an initial gap has to be left at the initially 'closed' state. This was the approach used by several researchers including Watton *et al.* [22, 23], and is adopted here. It is partially because of these drawbacks, the MV cannot fully close at the end of the diastole. Indeed, Griffith *et al.* [46], using a much refined adaptive mesh and second-order discretization of the immersed boundary model, showed that (a) the peak of the opening pressure drop is significantly reduced and that (b) the MV (Tube model) with bending stiffness closes better at the end of the diastole. However, even with the much refined Eulerian mesh, the MV could not close perfectly because a negative pressure gradient cannot be established at the end of the diastole when the flow rate boundary condition is applied (as here). This suggests that the presence of the flow vortex alone is not strong enough to aid the valve closure. However, from the point of view of assessing impact of the vortex structure on the valve behaviour, this model could provide us with some physical insights of the complex nature of the MV system.

5. CONCLUSION

The effect of the vortex flow induced by the LV model on the MV mechanics has been assessed in a three-dimensional dynamic fluid–structure interaction simulation using the IB method. Three

DOI: 10.1002/cnm

models are considered: the LV model in which the chordae are fully attached onto the moving LV wall, the LV Fixed-CAP model in which the MV is placed inside a moving LV, but the CAPs are fixed in space during the cardiac cycle, and the Tube model in which chordae are moving as if attached onto the LV wall, but the flow field downstream is a tube flow. Results show that the LV motion and the induced complicated flow pattern increase the opening pressure gradient. They also make the valve motion strongly asymmetric and increase the valve stretch in the commissural areas. At the early rapid filling phase, the flow is featured by a strong jet, which impinges on the LV wall and swirls around in a clockwise fashion, forming a main clockwise vortex in the z-plane. This vortex persists through the remaining of the diastole phase. This is significantly different to the flow in the Tube model, where the forward jet is accompanied by two vortices at each side.

The impact of the chordae attachment motion is also assessed and the results show that although the LV and the LV Fixed-CAP models yield very similar results in the flow field, the LV Fixed-CAP model has much smaller stretch in the chordae and the posterior leaflet. This suggests that if the papillary muscle can be kept to function (i.e. to compensate the chordae motion) in the MV implantation, it will release some valve and chordae stretches.

ACKNOWLEDGEMENTS

We are grateful for the funding provided by the British Heart Foundation, the Royal Society, and the Royal Academy of Engineering.

REFERENCES

1. Berne RM, Levy MN. *Principles of Physiology*. Mosby Elsevier Health Science: St. Louis, 1996.
2. Marzo KP, Herling IM. Valvular disease in the elderly. *Cardiovascular Clinics* 1993; **23**:175–207.
3. Roberts WC. Morphologic aspects of cardiac valve dysfunction. *The American Journal of Cardiology* 1992; **123**:1610–1632.
4. Galloway AC, Colvin SB, Baumann FG, Harty S, Spencer FC. Current concepts of mitral valve reconstruction for mitral insufficiency. *Circulation* 1988; **78**:1087–1098.
5. Waller BF, Howard J, Fess S. Pathology of mitral valve stenosis and pure mitral regurgitation—part II. *Clinical Cardiology* 1994; **17**:395–402.
6. Badduke BR, Jamieson WR, Miyagishima RT, Munro AI, Gerein AN, MacNab J, Tyers GF. Pregnancy and childbearing in a population with biologic valvular prostheses. *The Journal of Thoracic and Cardiovascular Surgery* 1991; **102**:179–186.
7. Zipes DP, Braunwald E. Heart disease. *A Textbook of Cardiovascular Medicine* (7th edn). WB Saunders Company: Philadelphia, 2005; 1603–1606.
8. Einstein DR, Kunzelman KS, Reinhall PG, Nicosia MA, Cochran RP. Non-linear fluid-coupled computational model of the mitral valve. *Journal of Heart Valve Disease* 2005; **14**:376–385.
9. Kunzelman KS, Cochran RP, Chuong C, Ring WS, Verrier ED, Eberhart RD. Finite element analysis of the mitral valve. *Journal of Heart Valve Disease* 1993; **2**:326–340.
10. Einstein DR, Kunzelman KS, Reinhall PG, Nicosia MA, Cochran RP. The relationship of normal and abnormal microstructural proliferation to the mitral valve closure sound. *Journal of Biomechanical Engineering* 2005; **127**:134–147.
11. Kunzelman KS, Quick DW, Cochran RP. Altered collagen concentration in mitral valve leaflets: biochemical and finite element analysis. *Annals of Thoracic Surgery* 1998; **66**:S198–S205.
12. Kunzelman KS, Reimink MS, Cochran RP. Annular dilatation increases stress in the mitral valve and delays coaptation: a finite element computer model. *Cardiovascular Surgery* 1997; **5**:427–434.
13. Cochran RP, Kunzelman KS. Effect of papillary muscle position on mitral valve function: relationship to homografts. *Annals of Thoracic Surgery* 1998; **66**:S155–S161.
14. Kunzelman KS, Reimink MS, Cochran RP. Flexible versus rigid ring annuloplasty for mitral valve annular dilatation: a finite element model. *Journal of Heart Valve Disease* 1998; **7**:108–116.

DOI: 10.1002/cnm

15. Reimink MS, Kunzelman KS, Cochran RP. The effect of chordal replacement suture length on function and stresses in repaired mitral valves: a finite element study. *Journal of Heart Valve Disease* 1996; **5**:365–375.
16. Lim KH, Yeo JH, Duran CM. Three-dimensional asymmetrical modeling of the mitral valve: a finite element study with dynamic boundaries. *Journal of Heart Valve Disease* 2005; **14**:386–392.
17. Prot V, Skallerud B, Holzapfel GA. Transversely isotropic membrane shells with application to mitral valve mechanics. Constitutive modelling and finite element implementation. *International Journal for Numerical Methods in Engineering* 2007; **71**:987–1008.
18. Maisano F, Redaelli A, Soncini M, Votta E, Arcobasso L, Alfieri O. An annular prosthesis for the treatment of functional mitral regurgitation: finite element model analysis of a dog bone-shaped ring prosthesis. *The Annals of Thoracic Surgery* 2005; **79**:1268–1275.
19. Votta E, Caiani E, Veronesi F, Soncini M, Montevecchi FM, Redaelli A. Mitral valve finite-element modelling from ultrasound data: a pilot study for a new approach to understand mitral function and clinical scenarios. *Philosophical Transactions. A Mathematical, Physical, and Engineering Sciences* 2008; **366**:3411–3434.
20. Votta E, Maisano F, Bolling SF, Alfieri O, Montevecchi FM, Redaelli A. The geoform disease-specific annuloplasty system: a finite element study. *The Annals of Thoracic Surgery* 2007; **84**:92–101.
21. Dal Pan F, Donzella G, Fucci C, Schreiber M. Structural effects of an innovative surgical technique to repair heart valve defects. *Journal of Biomechanics* 2005; **38**:2460–2471.
22. Watton PN, Luo XY, Wang X, Bernacca GM, Molloy P, Wheatley DJ. Dynamic modelling of prosthetic chorded mitral valves using the immersed boundary method. *Journal of Biomechanics* 2007; **40**:613–626.
23. Watton PN, Luo XY, Yin M, Bernacca GM, Wheatley DJ. Effect of ventricle motion on the dynamic behaviour of chorded mitral valves. *Journal of Fluids and Structures* 2008; **24**:58–74.
24. Kim WY, Walker PG, Pedersen EM, Poulsen JK, Oyre S, Houlind K, Yoganathan AP. Left ventricular blood flow patterns in normal subjects: a quantitative analysis by three-dimensional magnetic resonance velocity mapping. *Journal of the American College of Cardiology* 1995; **26**:224–238.
25. Bellhouse BJ. Fluid mechanics of a model mitral valve and left ventricle. *Cardiovascular Research* 1972; **6**:199–210.
26. Reul H, Talukder N, Muller EW. Fluid mechanics of the natural mitral valve. *Journal of Biomechanics* 1981; **14**:361–372.
27. Yoganathan AP, He Z, Jones SC. Fluid mechanics of heart valves. *Annual Review of Biomedical Engineering* 2004; **6**:331–362.
28. Weyman AE. *Principles and Practice of Echocardiography*. Lea & Febiger: Philadelphia, PA, 1994.
29. Baccani B, Domenichini F, Pedrizzetti G, Tonti G. Fluid dynamics of the left ventricular filling in dilated cardiomyopathy. *Journal of Biomechanics* 2002; **35**:665–671.
30. Long Q, Merrifield R, Xu XY, Kilner P, Firmin DN, Yang GZ. Subject-specific computational simulation of left ventricular flow based on magnetic resonance imaging. *Proceedings of the Institution of Mechanical Engineers, Part H: Journal of Engineering in Medicine* 2008; **222**:475–485.
31. Peskin CS. Flow patterns around heart valves: a numerical method. *Journal of Computational Physics* 1972; **10**:252–271.
32. Peskin CS. Numerical analysis of blood flow in the heart. *Journal of Computational Physics* 1977; **25**:220–252.
33. Peskin CS. The immersed boundary method. *Acta Numerica* 2003; **11**:479–517.
34. Peskin CS, McQueen DM. A three-dimensional computational method for blood flow in the heart. 1. Immersed elastic fibers in a viscous incompressible fluid. *Journal of Computational Physics* 1989; **81**:372–405.
35. Peskin CS, McQueen DM. Fluid dynamics of the heart and its valves, case studies in mathematical modeling. In *Ecology, Physiology and Cell Biology*, Othmer HG (ed.). Prentice-Hall: NJ, 1996; 309–337.
36. Wheatley DJ. Mitral valve prosthesis. *Patent Number WO03037227*, 2002.
37. Cronin R, Armour JA, Randall WC. Function of the in-situ papillary muscle in the canine left ventricle. *Circulation Research* 1969; **25**:67–75.
38. He Z, Sacks MS, Baijens L, Wanant S, Shah P, Yoganathan AP. Effects of papillary muscle position on in-vitro dynamic strain on the porcine mitral valve. *Journal of Heart Valve Disease* 2003; **12**:488–494.
39. Jimenez JH, Soerensen DD, He Z, Ritchie J, Yoganathan AP. Effects of papillary muscle position on chordal force distribution: an in-vitro study. *Journal of Heart Valve Disease* 2005; **14**:295–302.
40. Karas S, Elkins RC. Mechanism of function of the mitral valve leaflets, chordae tendineae and left ventricular papillary muscles in dogs. *Circulation Research* 1970; **26**:689–696.
41. Marzilli M, Sabbah HN, Lee T, Stein PD. Role of the papillary muscle in opening and closure of the mitral valve. *American Journal of Physiology-Heart and Circulatory Physiology* 1980; **238**:348–354.

DOI: 10.1002/cnm

42. Rayhill SC, Daughters GT, Castro LJ, Niczyporuk MA, Moon MR, Ingels NB, Stadius ML, Derby GC, Bolger AF, Miller DC. Dynamics of normal and ischemic canine papillary muscles. *Circulation Research* 1994; **74**:1179–1187.
43. Hammermeister KE, Warbasse JR. The rate of change of left ventricular volume in man. II. Diastolic events in health and disease. *Circulation* 1974; **49**:739–747.
44. He Z, Ritchie J, Grashow JS, Sacks MS, Yoganathan AP. In vitro dynamic strain behavior of the mitral valve posterior leaflet. *Journal of Biomechanical Engineering* 2005; **127**:504–511.
45. Pedrizzetti G, Domenichini F. Nature optimizes the swirling flow in the human left ventricle. *Physical Review Letters* 2005; **95**:108101.
46. Griffith BE, Luo XY, McQueen D, Peskin C. Simulating the fluid dynamics of natural and prosthetic heart valves using the immersed boundary methods. *Journal of Applied Mechanics* 2009; **1**:137–177.

DOI: 10.1002/cnm